Performance of a cryogenic silicon monochromator under extreme heat load

Aleksandr Chumakov,[a]*‡ Rudolf Rüffer,[a] Olaf Leupold,[a] Jean-Philippe Celse,[a] Keith Martel,[a] Michel Rossat[a] and Wah-Keat Lee[b,a]

[a]European Synchrotron Radiation Facility (ESRF), BP 220, 38043 Grenoble, France, and [b]Advanced Photon Source, Argonne National Laboratory, 9700 South Cass Avenue, Argonne, IL 60439, USA. E-mail: chumakov@esrf.fr

The performance of an indirectly cooled cryogenic silicon monochromator under heat loads up to 870 W has been studied. The investigation was performed over numerous parameters and included measurements of total flux, spectral density, rocking curves, angular beam profiles and crystal slope errors. An almost ideal monochromator performance was observed in the 270–570 W range of the heating power. At a heat load of ∼400 W and under standard operation conditions, the crystal distortions did not exceed 1 μrad. At the highest available heat load of 870 W, the crystal distortions were about 7 μrad.

Keywords: X-ray optics; cryogenic cooling; high-heat-load optics; silicon monochromators.

1. Introduction

The high flux of X-rays available at third-generation synchrotron radiation sources poses technical problems in handling the heat load. Modern undulator sources provide an X-ray beam with a power of about 1 kW. Without proper heat removal, such a beam easily melts tantalum and tungsten. X-ray optics, however, should not merely withstand the beam, but preserve a proper propagation of the radiation wavefront on the microradian level. This challenge is known as the heat-load problem at the third-generation synchrotron radiation sources.

The simple removal of ∼1 kW power can be easily achieved with water cooling. This, however, does not solve the problem. Local heating by a tiny X-ray beam leads to a temperature gradient and forms a bump on the crystal surface due to a non-homogeneous lattice expansion. The crystal surface deviates from a flat plane by a certain slope error δ, which is proportional to the beam power P according to

$$\delta \propto \Delta d \propto \alpha \Delta T \propto (\alpha/\kappa)P, \quad (1)$$

where α is the temperature expansion coefficient, κ is the thermal conductivity, ΔT is the temperature gradient and Δd is the variation of the lattice constant (Subbotin *et al.*, 1988). The ratio α/κ is the figure-of-merit parameter, which controls the crystal distortions at a given heating power. At room temperature the thermal expansion of silicon, $\alpha \simeq 2.6 \times 10^{-6}$ K^{-1}, is high enough to result in ∼200 μrad slope errors at a heat load of about 100 W (Marot *et al.*, 1992). A thermal bump with such a slope error decreases the reflection coefficient, makes the rocking curve broader and disturbs the propagation of the X-ray wavefront.

While water-cooled silicon monochromators have been implemented at some insertion-device beamlines at third-generation sources, these are always done in conjunction with other power- or power-density-reducing configurations, such as using a mirror upstream (Khounsary *et al.*, 1996) or using a grazing-incidence geometry (Ishikawa *et al.*, 1998). Having a mirror upstream is not feasible where higher energies (>20 keV) are needed and, in addition, one would need to deal with cooling the mirror. A tunable grazing-incidence geometry requires additional degrees of rotation for the monochromator. In this case, even at grazing incidence, enhanced heat transfer is required, which leads to more sophisticated coolant flow geometries, such as pin-post patterns. Unfortunately, the fabrication of these patterned crystals almost always leaves the crystal highly strained.

Another way to tackle the thermal expansion is to cool the silicon crystal down to 125 K, where silicon has zero thermal expansion (Bilderback, 1986). Under these conditions the temperature gradient causes much smaller distortions on the silicon surface, and the monochromator performance improves significantly (Marot *et al.*, 1992). Cryogenic silicon monochromators have been studied by the joint efforts of several synchrotron radiation facilities in the early 1990s, when the ESRF first faced the heat-load problem (Bilderback *et al.*, 2000). The cooling scheme was tested at several bending-magnet and wiggler sources of synchrotron radiation and revealed a proper performance up to a heating power of 140 W (Carpentier *et al.*, 2001). Today, cryogenic monochromators are installed at most undulator beamlines at the ESRF and at other synchrotron radiation facilities.

Going from a bending-magnet to an undulator source increases the heat load by an order of magnitude. How good the cryogenic monochromators work under these conditions is not clear. On the one hand, the directly cooled cryogenic monochromators reveal almost ideal rocking curves up to a heating power of 500 W (Lee *et al.*, 2000). The indirectly cooled monochromators do not show any flux losses at this heat-load level either (Tamasaku *et al.*, 2002). On the other hand, the rocking curves of the indirectly cooled monochromators reveal significant thermal distortions at 500 W (Zhang *et al.*, 2003) and even at 200 W (Lee *et al.*, 2001), which are partly confirmed by finite-element analysis (Zhang *et al.*, 2003).

The controversies in the experimental observations as well as the uncertainties in applications of the theoretical simulations may be attributed to a number of unknown parameters such as the heat-transfer coefficient. However, the principal question as to whether or not the cryogenic silicon monochromators can successfully cope with 500 W (the typical heat load at modern undulator beamlines) demands precise clarification. Moreover, progressive development of insertion devices as well as the foreseen augmentation of the storage-ring current (for instance, up to 250 mA at the ESRF) could make the heat-load problem more serious in the near future. If the application of cryogenic silicon monochromators is indeed restricted to a relatively moderate heat-load range, alternative solutions should be seriously investigated. This obviously would demand significant efforts and expenses; therefore, the high-power limits of acceptable performance of the cryogenic silicon monochromators merit careful reexamination.

2. X-ray source characteristics

The studies were performed at the nuclear resonance beamline ID18 (Rüffer & Chumakov, 1996) at the ESRF. It is one of the three most powerful beamlines at the ESRF. It is equipped with three 1.6 m-long undulators with 32 mm magnetic periods. The size of the X-ray beam within the central cone at the position of the entrance slit (28 m downstream of the center of the undulator straight section) is

‡ Also at Russian Research Center 'Kurchatov Institute', 123182 Moscow, Russia.

 © 2004 International Union of Crystallography DOI: 10.1107/S0909049503026785

1.2 mm × 0.6 mm (here and further on the widths are given in terms of horizontal × vertical full width at half-maximum sizes). At a nominal electron current of 200 mA and at the smallest allowed magnetic gap of ∼11 mm, the undulators provide ∼450 W in the central cone and ∼1000 W within a maximum aperture of 2 mm × 4 mm determined by the upstream front-end diamond window. The undulators are properly phased with respect to their magnetic period, although it does not influence the parameters of the X-ray beam very much owing to the finite spread of the electron energy (10^{-3}). The centers of the X-ray beams from all undulators are well aligned within the region of the central cone.

3. Cooling scheme

The high-heat-load monochromator at ID18 consists of two independent identical silicon crystals with a size of 80 mm (length) by 30 mm (width) by 40 mm (height). It operates in a vertical scattering geometry with Si *nnn* reflections, most commonly the Si 111. The surfaces of the crystals are cut asymmetrically to the Si (111) plane by 1° in order to match the angular acceptance of the Si 111 reflection in the 14–25 keV energy range to the vertical divergence (∼20 µrad) of the incident X-ray beam. These surfaces are mechanochemically polished down to 1.5 Å roughness (r.m.s.). Angular adjustment of the crystals is controlled by high-precision tangential bar stages (KOHZU) with ∼25 nrad accuracy of angular positioning.

Both crystals are cooled by liquid nitrogen in series according to the standard ESRF scheme (Marot *et al.*, 1992) (Fig. 1). The crystal is clamped between two copper heat exchangers by four M4 screws with spring washers. In order to minimize elastic deformations and to facilitate heat transfer, the side surfaces of the crystals and heat exchangers are polished and pressed to each other through 0.5 mm-thick indium foils. The interior of the heat exchangers is highly elaborated for efficient heat removal. Liquid nitrogen passes through 16 rectangular channels with a net surface area of as much as ∼200 cm^2. The total cross section of the channels (1.3 cm^2) matches the cross section of the half-inch tubes of the cooling loop. In normal operation, the cooling system works at a pressure of 3×10^5 Pa, a pressure drop of 0.4×10^5 Pa and a rotation frequency of the cryogenic pump of 45 Hz. These conditions correspond to a turbulent flow with a flow rate of 240 l h^{-1} (53 g s^{-1}) and a linear velocity of liquid nitrogen of 0.5 m s^{-1}. According to the Reynolds parameter, the transition from a laminar to a turbulent flow occurs at a frequency of the cryogenic pump of about 25 Hz. The crystal temperature is monitored using a Pt100 sensor located in a hole at the butt-end surface of the crystal. The cooling assembly is attached to the goniometer head through a rigid ceramic isolation plate.

The heat exchanger provides high cooling efficiency, comparable with that of directly cooled monochromators (Zhang *et al.*, 2003). By calculations, the effective heat-transfer coefficient on the 80 mm × 40 mm side surface of each heat exchanger is about 18 kW m^{-2} K^{-1}. This value, however, is somewhat lowered by the thermal resistance of the copper–indium–silicon interfaces.

Before installation of the crystals into the vacuum vessel of the monochromator, we checked (at room temperature) their deformation caused by clamping. The crystal was illuminated by a highly parallel (4 µrad divergence) beam of 14.4 keV radiation. The rocking curves of the Si 111 reflection were measured after each successive tightening of screws with a calibrated torque gauge. The results are shown in Fig. 2. Owing to the high collimation of the incident radiation, the rocking curves have an almost ideal 'Darwin table' shape. The shape does not change up to the highest applied torque of 15 dNm, which corresponds to a clamping pressure of 17×10^5 Pa. One could note a small stochastic variation of the rocking-curve width caused by the long angular drift of the crystal after each tightening (probably due to the elastic relaxation of the indium gasket).

4. Optics setup

Tests of heat-load effects have to be performed when the crystals are inserted into the vacuum vessel of the monochromator; therefore access to the crystals is limited. In order to study the performance of the monochromator we used the two optical schemes shown in Fig. 3. The first one (Fig. 3*a*) is a conventional scheme for rocking-curve measurements. The application of two detectors gives a convenient possibility of measuring rocking curves for two different radiation harmonics simultaneously. For instance, a calibrated ionization chamber monitors the rocking curve in the Si 111 reflection for relatively soft radiation. After passing the ionization chamber, the soft radiation is absorbed by an aluminium filter. Further downstream, an avalanche photodiode (Baron, 1995) serves to measure the rocking curve for *e.g.* third-harmonics radiation in the Si 333 reflection. The contributions of further higher-energy harmonics were reduced by an additional Nd_2O_3 absorber.

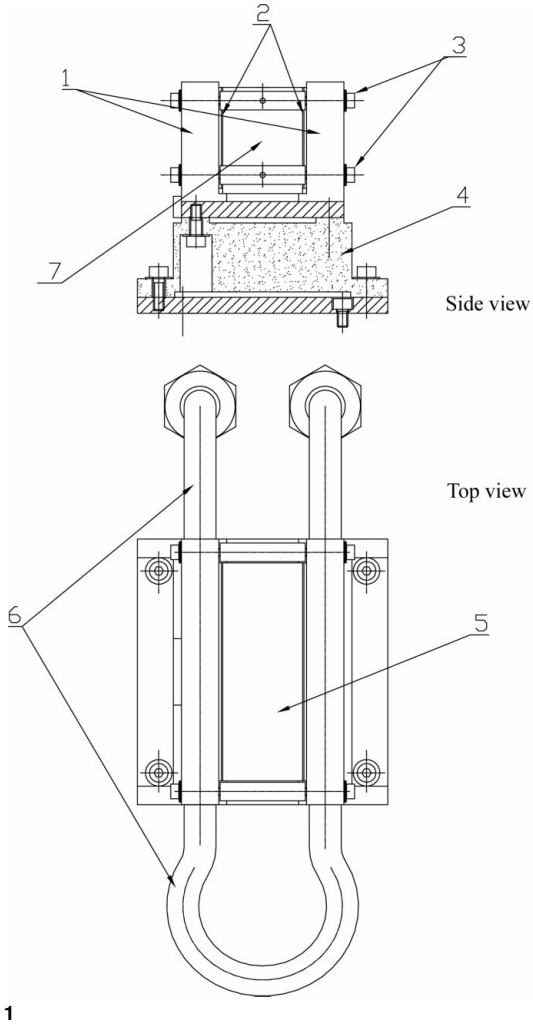

Figure 1
Scheme of the indirect cooling of the monochromator crystals. 1 – Copper heat exchangers; 2 – 0.5 mm-thick indium foils; 3 – four M4 screws to tighten the crystal between the heat exchangers; 4 – ceramic isolation; 5 – silicon crystal; 6 – copper tubes for liquid nitrogen; 7 – position of temperature sensor.

The second scheme (Fig. 3*b*) contains an additional high-energy-resolution monochromator with Si_3 and Si_4 silicon crystals, both in Si 975 reflection. For X-rays with 14.4 keV energy, it has an energy bandwidth of about 5 meV, which is almost three orders of magnitude less than the bandwidth of the high-heat-load monochromator (2.1 eV). Simultaneous monitoring of the flux after the high-heat-load monochromator and after the high-energy-resolution monochromator allows for parallel measurements of total flux and spectral density, respectively. Besides that, the second scheme permits measurements of the angular profile of the X-ray beam downstream of the monochromator (Baron *et al.*, 1999; Chumakov *et al.*, 2000). Rotation of the last crystal, Si_4, maps the angular density of the radiation with a magnification factor of two. Finally, as will be discussed below, a collimating compound refractive lens (Snigirev *et al.*, 1996) downstream of the high-heat-load monochromator allows for precise estimations of the slope error of the first crystal. In all the measurements performed in this work (except those discussed in §8), the secondary vertical slit S_2 is fixed at a gap of 1.0 mm.

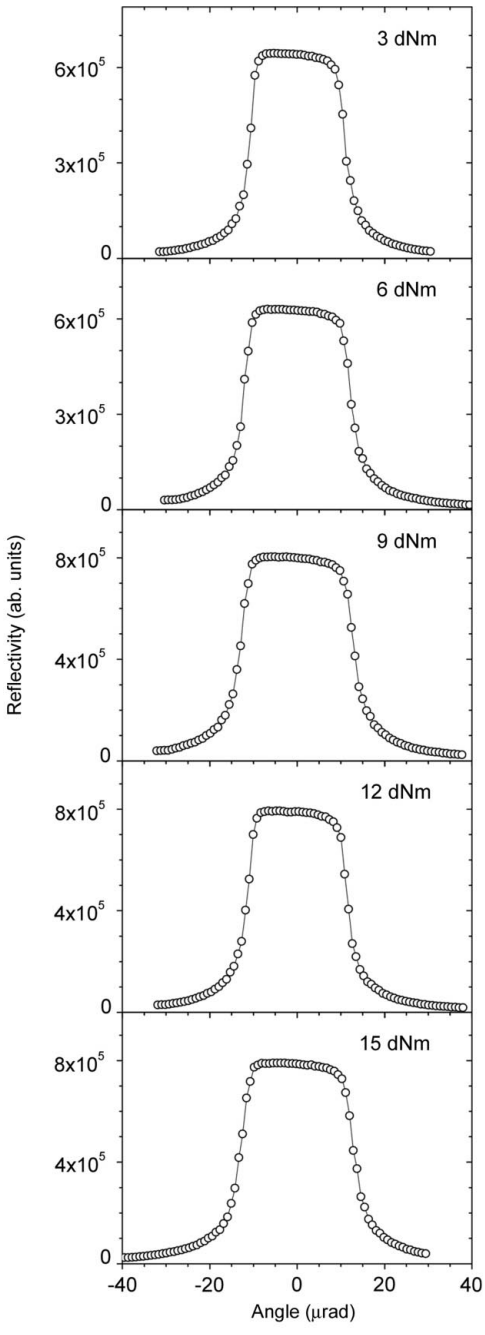

Figure 2
Monitoring the crystal quality during its tightening between the heat exchangers. The rocking curve of the Si 111 reflection for 14.4 keV X-rays was measured for increasing torque applied to the tightening screws. The incident radiation was collimated to ~4 μrad angular divergence. The solid line is to guide the eyes.

5. Vibration tests

Cryogenic cooling by liquid nitrogen can potentially degrade the monochromator performance due to flow-induced vibrations. Usual sources of vibrations are sharp bends of the coolant lines and undulating inner surfaces of flexible tubes, which can hardly be avoided in practice. In order to suppress vibrations, the crystals should be held as rigidly as possible, and the cooling system should be operated away from possible mechanical resonance frequencies.

In order to map the mechanical resonances, we measured rocking curves with 36 keV radiation in the Si 555 reflection as a function of the rotation frequency of the cryogenic pump. Under these conditions, the intrinsic width of the rocking curve is only 0.50 μrad, providing high sensitivity to additional vibrational broadening. Undulators were adjusted to third harmonics. In combination with the 555 reflection, this efficiently suppresses lower- and higher-energy harmonics. In addition, the contributions of the unwanted radiation harmonics were reduced by Al/Ta/Pt absorbers. These measurements were carried out under negligible heat load (5 W). In order to check the reproducibility of the results, two independent measurements (increasing and decreasing frequency) were performed (Fig. 4). We observed a wide frequency band of mechanical resonances in the 48–60 Hz frequency range and a few sharp resonances at 35, 64 and 74 Hz. At the worst point at 52 Hz, the rocking curve has two peaks separated by ~6 μrad (upper insert in Fig. 4). Such a shape is a typical feature for sinusoidal vibrations of a crystal, where the average

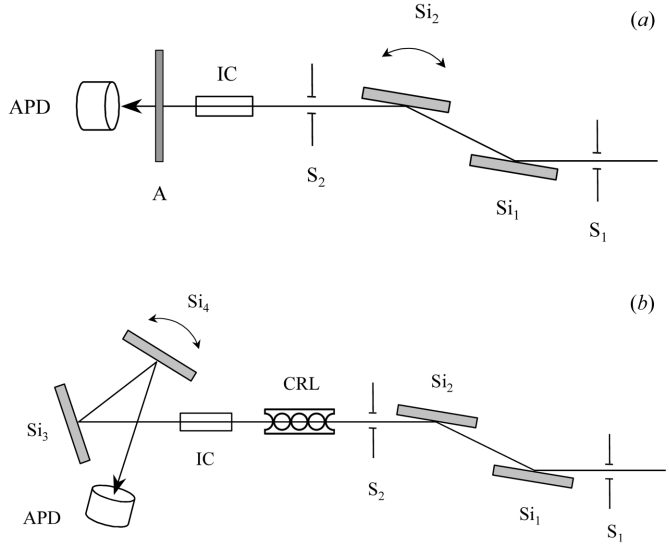

Figure 3
Optical schemes for measuring (*a*) rocking curves and (*b*) angular profile and spectral density of X-rays from the high-heat-load monochromator. S_1 and S_2 – two pairs of slits; Si_1 and Si_2 – Si *nnn* crystals of the high-heat-load monochromator; Si_3 and Si_4 – Si 975 crystals of the high-energy-resolution monochromator; IC – ionization chamber; A – absorbers; APD – avalanche photodiode detector; CRL – beryllium compound refractive lens (optional).

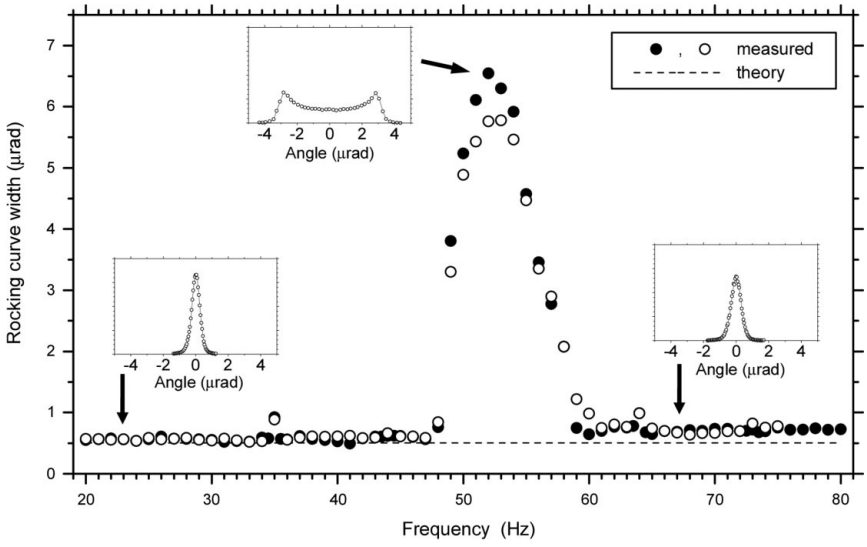

Figure 4
Measurements of the crystal vibrations induced by cryogenic cooling at a low (5 W) heat load. Solid and open circles show the results of two independent measurements of rocking-curve widths (FWHM) of the Si 555 reflection for 36 keV X-rays as a function of rotation frequency of the lquid-nitrogen cryogenic pump. The horizontal dashed line gives the theoretically expected value for ideal crystals. The left, right and upper insets show the rocking curves averaged over frequency ranges of 20–47 Hz and 61–80 Hz, and at 52 Hz, respectively. Solid lines in the inserts are to guide the eyes.

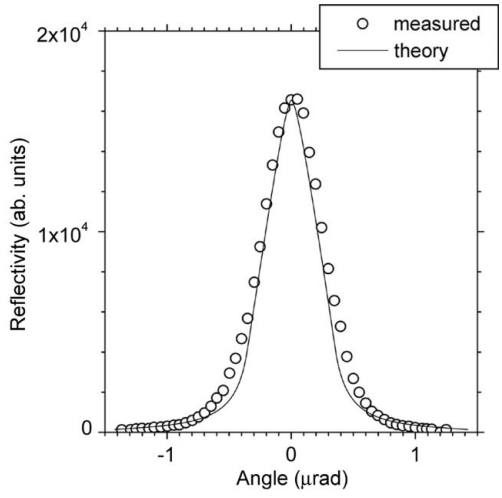

Figure 5
Rocking curve of the Si 555 reflection for 36 keV X-rays at low (5 W) heat load. The experimental data (circles) give the sum of 27 curves measured in the 20–47 Hz frequency range. The solid line shows a vertically scaled convolution of two reflectivity curves calculated for ideal crystals.

position is less probable than the extreme ones. Away from mechanical resonances, the rocking curve has a normal single-peak shape. The narrowest width was observed in the 20–47 Hz range. Fig. 5 shows a rocking curve, which is the average of 27 curves in this frequency range (excluding the 35 Hz point). Its width is 0.56 μrad, slightly broader than the theoretical one (0.50 μrad). Assuming Gauss-like shapes of the rocking curves, we estimate the additional broadening as $[(0.56\ \mu\text{rad})^2 - (0.50\ \mu\text{rad})^2]^{1/2} = 0.25\ \mu\text{rad}$. This is the value of the effective total crystal deformation (caused by vibrations and clamping) in the absence of a high heat load.

In order to investigate the evolution of the mechanical resonances with increased heat load, the vibration test was repeated at a heat load of 410 W (Fig. 6). Beyond the mechanical resonances, the rocking-curve width increases up to 1.8 μrad, revealing the heat-load effect. Somewhat larger broadening of the rocking curve below 30 Hz can be attributed to a laminar flow regime of liquid nitrogen at lower flow speed, which decreases the heat exchange efficiency as compared with a turbulent flow at higher frequencies. The sharp resonances at 35, 64 and 74 Hz are no longer seen because of the dominating heat-load effect. The main feature is the drastic growth of vibrations in the 48–60 Hz frequency range. We assume that it is caused by a kind of cavitation effect. For the further measurements, the frequency of the cryogenic pump was fixed at 45 Hz, where the influence of the mechanical resonances was negligible.

6. Investigation of the heat-load effect at constant current

In the normal mode of the ESRF operation, the electron beam current is almost constant. Under these conditions the heat load can be varied with filters, undulator gap or slit size. We performed two kinds of measurements: 'gap scan' and 'slit scans' (Fig. 7). During the 'gap scan' (solid circles), the 'white beam' slits S_1 were kept at a fixed size of 2 mm × 1 mm, slightly beyond the central cone (1.2 mm × 0.6 mm). The heat load was varied by closing the gaps of the undulators.

The 'gap scan' covers the heat-load range up to 340 W. Further increase of the heat load was achieved with 'slit scans'. In the 'slit scans', the undulators were adjusted to an odd harmonic at a smallest gap of ∼11 mm. The heat load was varied by opening the vertical slit at various sizes of the horizontal slit (open symbols).

The crystal distortions were monitored by simultaneous measurements of the rocking curves for the 14.4 keV radiation in the Si 111 reflection and for the 43.2 keV radiation in the Si 333 reflection. The absorbed power of synchrotron radiation was derived from the temperature difference of liquid nitrogen before and after the

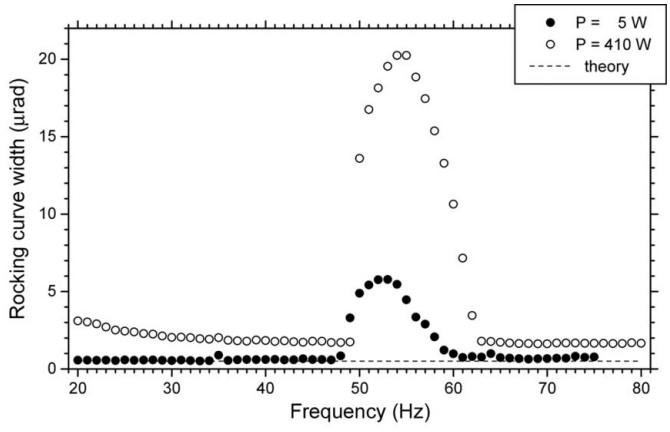

Figure 6
Amplification of resonance vibrations of the monochromator crystals by high heat load. Solid and open circles show rocking-curve widths (FWHM) of the Si 555 reflection for 36 keV X-rays with 5 W and 410 W heat load, respectively. The horizontal dashed line shows the theoretical value of the unperturbed width.

monochromator assuming the known flow rate of 240 l h^{-1}, and density and heat capacity (C_P) of liquid nitrogen of 28 mol l^{-1} and 58 J mol^{-1} K^{-1}, respectively.

Fig. 7(*a*) shows that the significance of the heat-load effects for the Si 111 reflection of the 14.4 keV radiation is negligibly small. The rocking-curve width does not change with the heat load up to 870 W. It remains around 24.1 $\pm$ 1 µrad, which is slightly larger than 22.8 µrad expected from a convolution of two rocking curves calculated for an ideal silicon crystal at 125 K. We do not have an explanation for this discrepancy, but it probably should not be attributed to drawbacks in the monochromator performance in view of the results discussed below.

The narrower Si 333 reflection of the 43.2 keV radiation (intrinsic width of 1.4 µrad) is more sensitive to heat-load effects. Fig. 7(*b*) shows that the thermal distortions do vary with the heat load. Moreover, at equal heat load, they strongly depend on the slit size.

The two-dimensional analysis of the slit size–heat load dependence of the rocking-curve width (not discussed here for shortness) leads to the following observations:

(i) At the points where the 'slit scans' (open symbols) cross the 'gap scan' (solid circles), they correspond to a vertical size of 1 mm, the same as during the 'gap' scan. This means that the vertical slit size and the heat load are the two parameters which entirely define the crystal distortions, regardless of the undulator gap and the horizontal slit size.

(ii) Within the 270–570 W power range, the rocking-curve width almost loses dependence on the heating power and depends mainly on the vertical beam size. For instance, at 1 mm vertical slit size the rocking-curve width stays around 1.7 µrad between 250 and 340 W (solid circles). The lower arrows show the data for a 1.5 mm vertical slit size. Here the rocking curve has an approximately identical width of 3 µrad at 320 and 440 W. The upper arrows indicate the data for a 2 mm vertical slit size. Here the width of the rocking curve remains close to 4.5 µrad at 270, 400 and 570 W.

(iii) Within the 270–570 W power range, the broadening of the rocking curve saturates with vertical slit size. The rocking-curve width stays almost constant at 4 µrad (open squares) or 5 µrad (open triangles), whereas the heat load continuously grows.

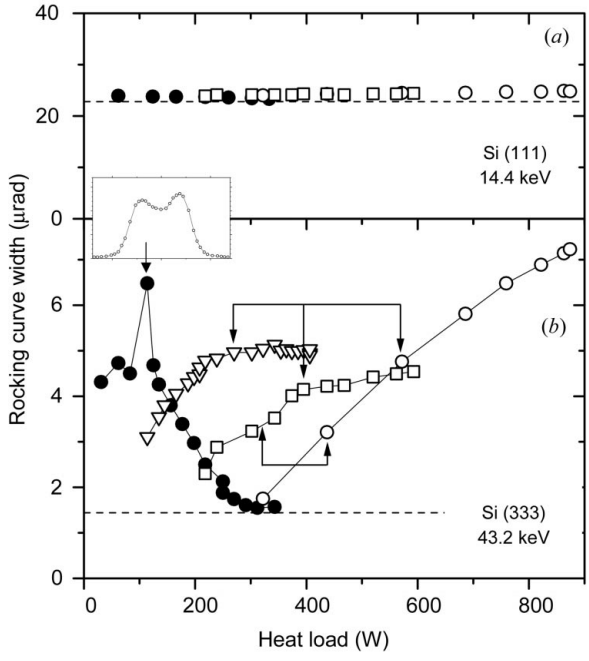

Figure 7
Rocking-curve width (FWHM) of (*a*) the Si 111 reflection for 14.4 keV and (*b*) the Si 333 reflection for 43.2 keV X-rays as a function of heat load. The heat load was varied in 'gap scan' (solid circles) by closing the undulator gaps with the fixed size of the vertical slit of 1 mm and in 'slit scans' (open symbols) by opening the vertical slit with the fixed size of the horizontal slit of 2 mm (circles), 1.5 mm (squares) and 1 mm (triangles). The dashed lines show the rocking-curve widths calculated for ideal crystals. The solid lines are to guide the eyes. The lower and upper arrows indicate the data points measured at identical vertical slit sizes of 1.5 and 2 mm, respectively. The insert shows the rocking curve at a heat load of 114 W.

These observations can be explained by a combination of two effects: the evolution of the thermal bump according to the mean temperature of the crystal surface and the displacement of the bump relative to the spot of the monitored radiation. The first effect is controlled by the temperature dependence of the figure-of-merit parameter α/κ. The thermal expansion α is close to zero at a heat load of about 250–600 W (because in this region the crystal distortions almost do not depend on heating power). This power range corresponds to the 'transition region' (Zhang *et al.*, 2003). More precisely, the exact zero expansion is reached probably at 340–440 W, where the smallest distortions are observed for any fixed slit size. Below 300 W, the 'gap scan' data (solid circles) show an increase of thermal distortions caused by the negative thermal expansion.

The second effect consists of the displacement of the thermal bump relative to the spot of the monitored radiation. An important issue is that the measured slope errors should not be attributed to the entire surface of the thermal bump: the monitored X-rays are limited either to the central cone ($\sim$0.6 mm) or to the 1 mm vertical secondary slit.

The thermal bump has three distinct regions: (*a*) at the tails, where the slope changes from near zero to some value, (*b*) at the sides, where the slope is fairly constant, and (*c*) near the peak, where the slope changes rapidly, going from positive to negative as it crosses the center. Because the heat is provided mainly by the high-energy radiation and because of the extinction effect, power penetration to the silicon crystal is deeper than the penetration of the monitored radiation. This causes the thermal bump to be displaced towards the downstream side of the actual beam footprint on the crystal surface (Chrzas *et al.*, 1990; Mocella *et al.*, 2003). Thus, when the vertical slit matches the central cone size, the spot of the monitored radiation is located on the relatively flat upstream side of the thermal bump. Opening the vertical slits increases the size of the thermal bump but not the monitored radiation spot. Therefore, the spot of the monitored radiation effectively becomes closer to the centre of the thermal bump where the changes in slope are larger. This leads to the broader rocking curve. For instance, at a fixed heat load of 270 W, opening of the vertical slit from 1 to 2 mm increases the rocking-curve width by a factor of three (Fig. 7*b*). Once the spot of the monitored radiation is in the linear change-in-slope region near the centre of the bump, the measured distortions remain constant. In addition, since during the 'slit scans' the increase in power is not accompanied by higher power density, the actual slopes at the center of the thermal bump do not change much. This explains the saturation of the rocking-curve broadening at large vertical slit sizes.

Thus, the effective crystal distortions are controlled by two parameters: the heat load and the vertical slit size. In particular, opening of the vertical slit deteriorates the monochromator performance even if the heat load is kept constant. Therefore, the investigations of the heat-load effects with the 'slit scans' produce a kind of an artifact: the dominating effect of the thermal bump displacement can overcome the smaller (or even opposite) effect of its height variation (compare the results of the 'slits scans' and 'gap scan' in Fig. 7*b*). In order to exclude the effect of the slit size, proper estimation of the high-power

limits of the monochromator performance must be performed under standard operation conditions, with the fixed vertical slit opened only slightly beyond the central cone, *i.e.* up to 1 mm in the present work.

At a vertical slit size of 1 mm the rocking curve in the zero thermal expansion region (at 310 W) reaches the lowest width of 1.6 μrad. Assuming, as above, Gauss-like shapes of the distorted and ideal rocking curves, we estimate the thermal-induced broadening as $[(1.6\ \mu\text{rad})^2 - (1.4\ \mu\text{rad})^2]^{1/2} = 0.8\ \mu\text{rad}$. At lower heating power, the evolution of the thermal distortions is properly displayed by the 'gap scan' data because they are taken at a fixed vertical slit size of 1 mm and, as discussed above, do not depend on the undulator gap and horizontal slit size. At higher heat load, the data are available only for bigger slit sizes. At the highest heating power of 870 W, the rocking-curve width reaches 7 μrad at a vertical slit size of 4 mm. On the basis of the present results we cannot unambiguously predict how well the monochromator would perform if the entire power of 870 W were concentrated within a 1 mm vertical aperture. On average, the temperature of the crystal surface and, therefore, the figure-of-merit parameter α/κ should probably not change much because the redistribution of power does not affect the overall thermal balance. Locally, however, the higher power density will obviously increase both the peak temperature and the temperature gradient. This should result in a stronger thermal bump and, consequently, a poorer monochromator performance. On the other hand, as discussed above, with a small vertical slit the spot of the monitored radiation will be located within the less disturbed side-part of the thermal bump. Therefore, an opposite effect of the improved performance might also be possible.

Artifacts in the effective crystal distortions can appear not only in the 'slit scans' but, in general, in the 'gap scans' as well. Detuning of the undulators from odd harmonics spreads the monitored radiation out of the central cone, where it is reflected by the more curved parts of the thermal bump. This effect is not significant for the 'gap scan' data in the 125–340 W range, where one undulator was kept adjusted to an odd harmonic. Therefore, it always provided the monitored radiation with a proper spatial distribution within the central cone region, whereas the relative intensity of the monitored radiation from the two other detuned undulators was negligibly small. In contrast, the data at lower heat load were obtained only with one undulator, whereas two others were entirely open. Therefore, below 125 W the distribution of the monitored radiation over the thermal bump could not be controlled. The exceptionally unfavorable pattern of the monitored radiation obviously appeared at 114 W, where the undulator was detuned slightly (0.9 mm) above the proper gap. At this point we reproducibly observed an exceptionally broad (7 μrad) rocking curve with a double-peak shape (insert in Fig. 7).

7. Investigation of the heat-load effect as a function of the storage-ring current

The results discussed in the previous section show that unambiguous measurements of the heat-load effects should be performed with optimized and fixed undulator gaps and slit size. In this case, a variation of the heat load can only be achieved by a variation of the electron beam current of the storage ring. At our request, the machine division of the ESRF supported these studies and ramped the storage-ring current from 20 up to 200 mA in steps of 20 mA. (As a collateral effect, the electron beam vertical emittance decreased from 7 nm to 2 nm. This, however, had negligible influence on the monochromator performance.) The results discussed below were obtained during this mode of operation with optimized and fixed undulator gaps and a fixed S_1 slit size of 2 mm × 1 mm.

Fig. 8(*a*) shows the incident (solid line) and absorbed (open circles) power of synchrotron radiation as a function of the storage-ring current. The incident power was calculated using the *SWR* code (Chubar & Elleaume, 1998) and corrected for the small attenuation by the 300 μm-thick front-end diamond window (∼10%). The absorbed power was derived from the temperature difference of liquid nitrogen before and after the monochromator as discussed above.

The crystals of the monochromator are sufficiently large to absorb the incident radiation entirely. For instance, the transmission coefficient for radiation with energy up to 50 keV is less than 10^{-2}. Therefore, the difference between the incident and absorbed heat load should be almost negligible. This is indeed revealed by Fig. 8(*a*). A small (∼10%) discrepancy can be possibly attributed to some radiative power losses due to Compton scattering *etc*.

At the highest storage-ring current of 200 mA, the heat load reaches 400 W. According to calculations, the power density is mostly flat within the entrance slit of 2 mm × 1 mm. Average and peak values are 200 and 210 W mm^{-2}, respectively. By calculations, the power absorbed in the first 10 μm of silicon thickness along the beam was ∼4 W.

Fig. 8(*b*) shows the variation of the crystal temperature with the storage-ring current. The temperature at the hot spot on the top surface of the crystal was not accessible experimentally. The reported data give the temperature at the butt-end surface of the crystal (Fig. 1). With the rise of the storage-ring current, the temperature increases linearly. In general, these data together with the parameters

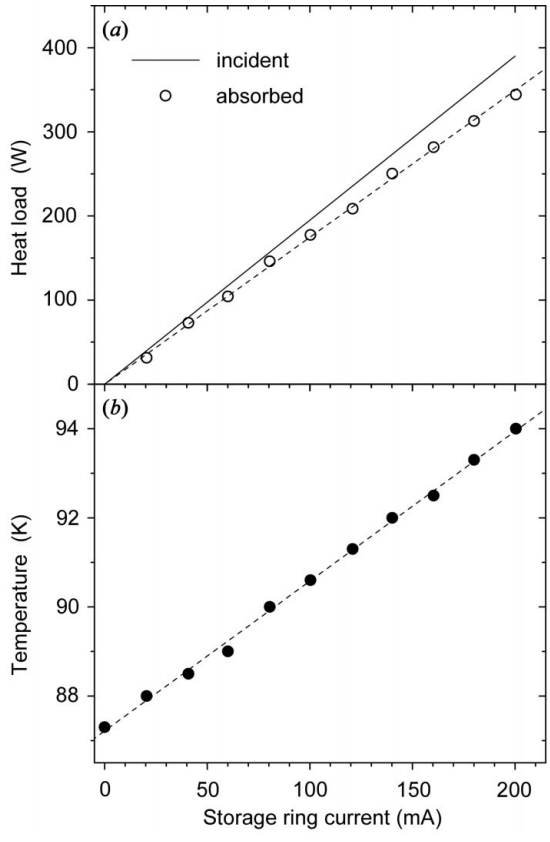

Figure 8
(*a*) Calculated incident (solid line) and measured absorbed (open circles) power of synchrotron radiation, and (*b*) temperature of the first monochromator crystal at the butt-end surface (solid circles) as a function of the storage-ring current. The dashed lines are linear fits.

of the cooling scheme mentioned above could be used to estimate the temperature of the hot spot. More practically, they provide a useful reference so that under different heat load the crystal can be maintained at the desired temperature by adjusting the cryogenic pump parameters. In this way the optimal regime of the monochromator performance can be adjusted to various electron beam currents of the storage ring.

A practical criterion for judging an absence of heat-load effects is the linearity of radiation flux with the storage-ring current. Fig. 9(*a*) shows the total flux of the 14.4 keV radiation within the energy bandwidth of 2.1 eV of the double Si 111 reflection measured with the calibrated ionization chamber. The dependence is exactly linear and does not reveal any significant heat-load effects. At a nominal current of 200 mA, the radiation flux reaches 6×10^{13} photons s^{-1}. To our knowledge, it is one of the highest intensities of monochromatic X-rays ever obtained.

The value of the total flux, however, has to be treated with care. For a distorted crystal the decrease of the reflection coefficient is usually accompanied by a rocking-curve broadening. Thus, the losses in the spectral density can be compensated for by an increase in the energy bandwidth. The evolution of the spectral density with the storage-ring current is, therefore, the more sensitive and conclusive parameter. Fig. 9(*b*) shows the spectral density of the 14.4 keV radiation measured as the photon flux after the high-energy-resolution monochromator in the energy bandwidth of ~5 meV (Fig. 3*b*). The data are not corrected for a finite angular acceptance of the high-energy-resolution monochromator and, therefore, give not an absolute but a relative value of the spectral density. Similar to the total flux, the spectral density increases monotonically with the storage-ring current. The slope, however, becomes steeper at a heat load of 250 W. This 'inverse' heat-load effect is consistent with the above-discussed best performance of the monochromator in the 250–600 W range.

Fig. 10 shows the rocking-curve width of the 14.4 keV radiation in the Si 111 reflection as a function of the heat load. Similar to the preliminary measurements at constant storage-ring current (Fig. 7), the data do not vary with heat load, indicating that the possible distortions caused by the heat load are much less than the sensitivity of these measurements. More sensitive data with 43.2 keV radiation and the Si 333 reflection could not be obtained because of the short time available in this special mode of storage-ring operation.

Another approach for monitoring the effects of a high heat load is to investigate the radiation wavefront downstream of the heat-load monochromator. This technique is somewhat more complicated than rocking-curve measurements; therefore, it is not commonly used for the characterization of high-heat-load monochromators. It requires two additional crystals with high-order reflection, preferably identical ones (Baron *et al.*, 1999; Chumakov *et al.*, 2000). The scheme, therefore, is identical to the one used for monitoring the spectral density (Fig. 3*b*). The first crystal Si_3 of the high-energy-resolution monochromator prepares a fan of X-rays where the angular direction of some spectral component correlates with its energy. Both the divergence and the spectral width of the fan are proportional to the angular divergence of the X-ray beam after the high-heat-load monochromator. The rocking curve of the last crystal Si_4 measures this divergence with a proportionality factor dependent on the Bragg angles of both crystals. In the easiest case of identical crystals, the angular scan of the Si_4 crystal maps the angular profile of the X-ray beam incident on the Si_3 crystal with a magnification factor of 2.

In the absence of heat-load effects, the monochromator crystals are flat and the angular profile of X-rays downstream of the high-heat-load monochromator is identical to that of the incident X-rays. When the crystal is deformed by heat load and its surface deviates from flat by some particular slope error angle δ, the reflected beam deviates from its primary direction by an angle 2δ. Therefore, the increase in the angular width of the X-ray beam after the crystal gives a measure of the slope error caused by the heat load with a magnification factor of 2. However, we can access the X-ray beam only downstream of the monochromator after an additional reflection by the second crystal. The angular profile of the X-ray beam after the second crystal is controlled by the product of the angular dependencies of reflectivity

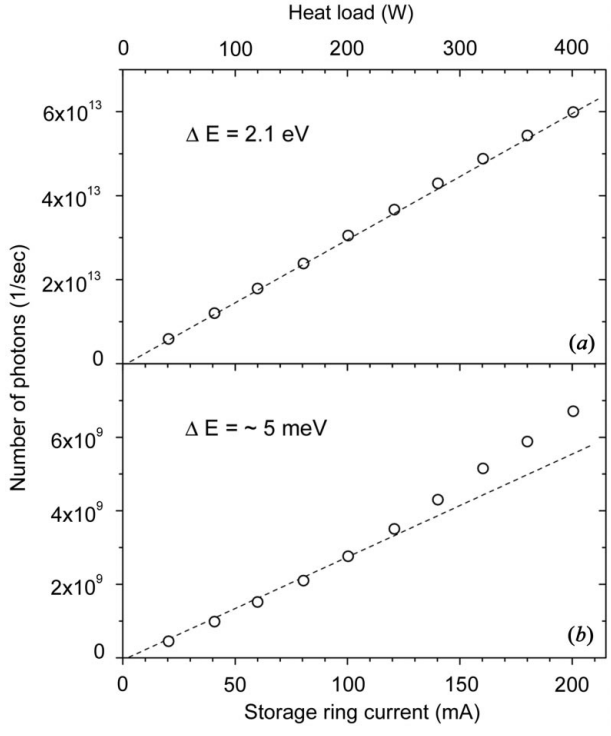

Figure 9
Measurements of (*a*) flux and (*b*) spectral density of the X-ray beam from the high-heat-load monochromator as a function of electron current in the storage ring. Dashed lines are to guide the eyes. The upper horizontal axis shows the calculated heat load.

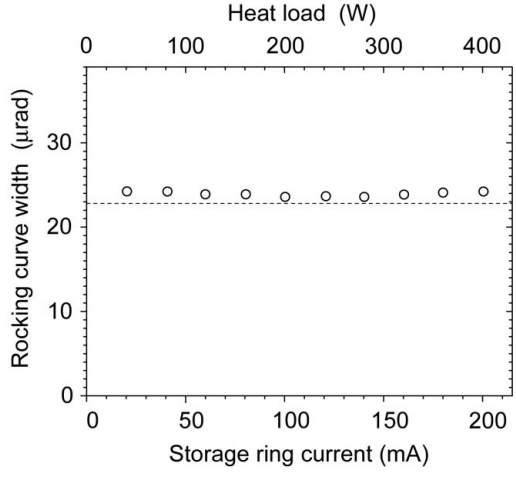

Figure 10
Rocking-curve width (FWHM) of the Si 111 reflection of 14.4 keV X-rays as a function of electron current in the storage ring. The dashed line shows the theoretical value calculated for an ideal crystal. The top axis shows the calculated heat load.

of the first and the second crystal and, thus, the picture becomes more complicated. Using numerical simulations we found that for a slope error δ smaller than the rocking-curve width, the angular displacement $\Delta\theta$ of the X-ray beam after the second reflection varies in the $\delta < \Delta\theta < 2\delta$ range. Thus, similar to a single-crystal reflection, the angular profile of the X-ray beam downstream of the double-crystal monochromator provides a measure of the slope error of the first crystal, though the magnification coefficient is not equal to 2 exactly. In particular, it is close to 2 when the angular shift $\Delta\theta$ is smaller than half of the rocking-curve width.

Fig. 11(*a*) shows the width of the angular profile of the 14.4 keV X-rays downstream of the monochromator (the lens was removed from the beam) as a function of the heat load. It varies only slightly with heat load and approaches the expected value of 21 μrad at heat loads above 300 W.

The sensitivity can be tremendously increased by inserting a collimating refractive lens into the beam downstream of the monochromator. The focal length of the lens matches the distance L to the radiation source (to the center of the straight section). Therefore, it prepares an almost parallel beam of X-rays with a vertical divergence of less than 1.7 μrad (Chumakov *et al.*, 2000). Consider a point on the first crystal, which is seen from the radiation source at an angle α. Suppose that at this point the crystal surface deviates from flat by a slope error δ. The reflected beam acquires an angular shift of 2δ, leading to a relative displacement of an imaginary source point from the real one by

$$\Delta L/L = 2\delta/\alpha. \quad (2)$$

Using the equation of a thin lens, we find an additional broadening $\Delta\theta$ of the X-ray beam after the lens as

$$\Delta\theta \simeq 2\delta. \quad (3)$$

In contrast to the previous measurements of the angular profile without the lens, this broadening can be observed at 'zero background', without an additional contribution of the primary divergence of the X-ray beam. In practice, as discussed above, the proportionality coefficients of 2 in equations (2) and (3) can be somewhat smaller because of the additional reflection by the second crystal.

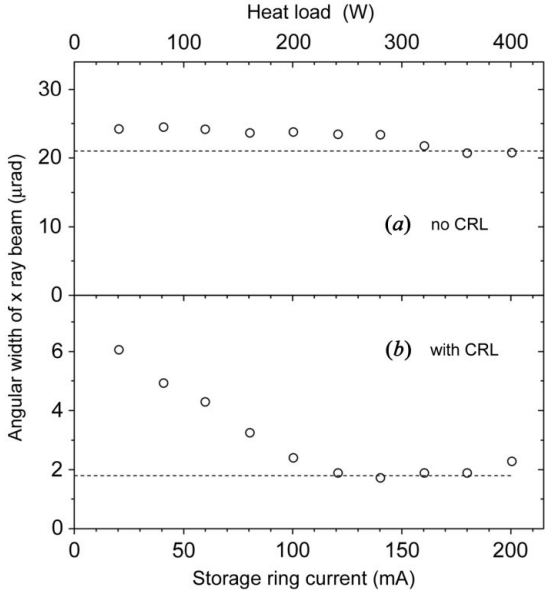

Figure 11
Angular width (FWHM) of the 14.4 keV X-ray beam from the high-heat-load monochromator (*a*) without and (*b*) with additional collimation by a compound refractive lens. The dashed lines show (*a*) the expected width of the X-ray beam and (*b*) the resolution of angular profile measurements. The top axis shows the calculated heat load.

The width of the angular profile of the 14.4 keV radiation after the collimating lens is shown in Fig. 11(*b*). At low heating power, it decreases with the storage-ring current. As discussed above, the crystal surface is close to the temperature of zero thermal expansion in the heat-load range 250–600 W and reaches it exactly at about 340–440 W. Consistently, in the 240–400 W range of the heat load the width of the angular profile reaches the limit of the angular resolution of the present optical scheme (1.8 μrad) and stays almost constant. In this region the largest width of the beam profile of 2.3 μrad was observed at 400 W. From this value we estimate the thermal-induced broadening of the beam profile as $\Delta\theta = [(2.3\ \mu\text{rad})^2 - (1.8\ \mu\text{rad})^2]^{1/2} = 1.4\ \mu\text{rad}$. Within the entire range of the heat load, the beam profile is narrower than the half of the intrinsic rocking-curve width (22.8 μrad). Therefore, according to the discussion above, the proportionality coefficient in equation (3) should be close to 2. Thus, the effective slope error δ of the first crystal does not exceed 3 μrad at lowest and 0.7 μrad at highest heat load.

8. Direct measurements of the slope error

The results discussed above give a weighted estimate of the slope error of the first crystal averaged over the spot of the monitored radiation. More detailed information can be obtained by space-differential measurements (Oversluizen *et al.*, 1989; Berman & Hart, 1991). The simplest way to do so would be to scan a narrow first slit (S_1) vertically and to measure at each point the angular direction of the X-ray beam after the monochromator. This, however, would modify the heat load and, therefore, is unacceptable. We have performed these measurements by scanning the second slit (S_2) while keeping the first one (S_1) constant (2 mm × 1 mm). Thus, various parts of the first crystals were examined looking through the downstream slit. As long as the values of the slope error are small, this approach is equivalent to the first one. It gives differential measurements in the vertical plane, though the data are still averaged in the horizontal plane.

The measurements were performed at a heat load of 290 W. A 100 μm-high second slit was scanned vertically in the ±0.5 mm range (the vertical size of X-ray beam at the slit position was 0.6 mm). For each point the vertical angular direction of the X-rays downstream of the monochromator was measured by rocking the Si_4 crystal (see Fig. 3*b*). In the absence of a heat bump, the angular direction as a function of the slit position should give a linear plot with the slope equal to the inverse distance from the slit to the radiation source. If the heat load causes a bump on the crystal surface with an ideal parabolic shape, the linear plot would persist; however, the effective distance to the source will change according to equation (2). For a non-parabolic-shaped bump, the plot would deviate from the ideal linear dependence. The results are shown in Fig. 12(*a*). The best linear fit was obtained with an effective slit–source distance of 32.43 ± 0.30 m, which is only different by 2 cm from the real distance of 32.45 ± 0.02 m. In the model of an ideal parabolic shape of the thermal bump, we estimate from equation (2) the mean slope error as ±0.1 μrad assuming the largest possible variation of the slit–source distance of 0.3 m and a characteristic angle α of ±10 μrad. The deviations from the linear fit (Fig. 12*b*) give a more reasonable estimate of the slope error of about 0.7 μrad.

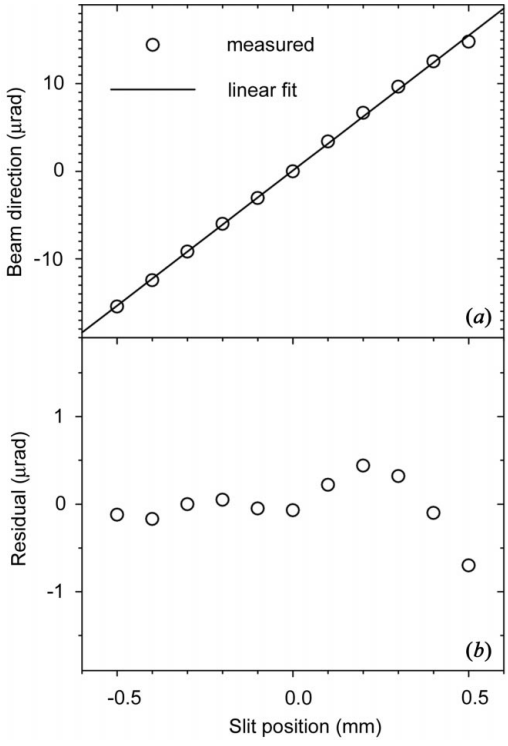

Figure 12
Measurements of the wavefront distortion at a heat load of 290 W. (*a*) The vertical angular position of the reflected 14.4 keV X-ray beam is plotted as a function of the vertical position of the second slit. The solid line is a linear fit. (*b*) Difference between the experimental data and the linear fit.

9. Conclusions

We have investigated the performance of an indirectly cooled silicon monochromator under heat-load power and peak power density up to 870 W and 210 W mm^{-2}, respectively. The crystal assembly and cooling system were adjusted to avoid elastic deformations and vibrations. The net broadening of the rocking curves due to both vibrations and mounting-induced deformations did not exceed 0.25 μrad.

At equal heat load, the performance of the monochromator strongly depends on the vertical slit size. We attribute this effect to a displacement of the thermal bump relative to the spot of the monitored radiation. The best performance, fortunately, corresponds to the standard operation conditions, where the slit aperture is slightly bigger than the central cone of the monitored radiation.

In preliminary measurements with almost constant electron beam current the monochromator showed the best performance in the heat-load range 250–600 W. More precisely, the crystal surface reaches the temperature of zero thermal expansion at about 340–440 W. At 340 W and under standard operation conditions the thermal-induced broadening of the rocking curves did not exceed 0.8 μrad.

The absence of significant thermal distortions was confirmed in studies of the monochromator performance as a function of the electron beam current. The total flux and the spectral density of 14.4 keV radiation in the Si 111 reflection increased almost linearly with the storage-ring current and gave no indication of losses up to a heat load of 400 W. Measurements of the angular profile of the X-ray beam collimated by a compound refractive lens gave the estimation of the effective slope error of the crystal surface as about 0.7 μrad at a heat load of 400 W. The same estimate was obtained with the space-angle differential measurements of the radiation wavefront at a heat load of 290 W.

Thus, we observed only negligibly small deviations of the monochromator performance from the ideal one. The thermal-induced distortions of the crystal surface were not seen with the usually sufficient accuracy of a few arcseconds. They were still at the limit of visibility even with the ∼μrad resolution and amounted to ∼0.8 μrad within the 240–400 W heat-load range and 7 μrad at the highest available heat load of 870 W. These distortions are much smaller than earlier reported observations for similar indirectly cooled monochromators (Lee *et al.*, 2001; Zhang *et al.*, 2003) and at least as good as those for directly cooled devices (Lee *et al.*, 2000).

There are two explanations for the smaller crystal distortions observed in this work. Firstly, the main improvement of the present monochromator appears to be the higher heat-transfer coefficient of the cooling scheme. Indeed, the region of zero thermal expansion in the present work is reached at a higher heating power relative to similar studies by Lee *et al.* (2001). It also seems to be spread over a wider heat-load range in comparison with the recent results of Zhang *et al.* (2003). Secondly, almost all measurements in this work were performed under standard operation conditions, *i.e.* with undulators adjusted to odd harmonics. Under these conditions the monitored radiation illuminates a relatively small part of the thermal bump (corresponding to the ∼0.6 mm-high central cone of the undulators) regardless of the actual size of the entrance slit. Furthermore, in most of the measurements we avoided excessive opening of the entrance slit beyond the central cone, keeping the radiation spot within the relatively flat side-part of the thermal bump. Thus, the effective crystal distortions measured in this work correspond only to a fraction of the actual distortion over the entire thermal bump and, most often, to the less distorted fraction. In contrast, the works of Lee *et al.* (2001) and Zhang *et al.* (2003) focused on measurements of the total effective distortions over the entire thermal bump. That was accomplished by the use of off (non-odd) harmonics of the undulators.

Similar reasons can also explain the deviation of the present results from the theoretical predictions. Most finite-element studies (Zhang *et al.*, 2001, 2003) state peak-to-valley values of slope errors over the beam footprint along the centerline where the distortions are largest. In experiments, however, measurements usually average at least over the transverse (horizontal) direction. This difference has been already elucidated by Tajiri *et al.* (2001). Furthermore, finite-element studies tend to treat the monochromators as mirrors and assume a purely geometrical ray approach. While this simple model is fine for small slope errors, it breaks down for large distortions (Mocella *et al.*, 2003).

In summary, the results show that up to the peak power density of 210 W mm^{-2} the indirectly cooled silicon monochromators can provide an ideal performance up to a heat load of 400 W and an acceptable performance at 900 W. Predictions of the performance at higher heat-load density are not straightforward. Nonetheless, the results suggest that a cryogenic silicon monochromator is not yet at its limits.

The authors acknowledge the help of the ESRF technical support groups for installation and maintenance of the liquid-nitrogen cooling system. We thank P. Elleaume, L. Hardy and J.-L. Revol for implementation of the special mode of the storage-ring operation; J.-P. Vassally, P. Villermet, A. Rommeveaux, O. Hignette and A. Freund for preparation and characterization of silicon crystals; J. Chavanne and C. Penel for undulator maintenance; A. Rogalev, L. Leclerc and

C. Schulze-Briese for technical consulting; and L. Zhang for fruitful discussion. The APS is supported by the US Department of Energy, Office of Basic Energy Sciences, under Contract No. W-31-109-Eng-38. AC thanks O. Chubar for guidelines in using the *SWR* code and J. Arthur for an introduction to the field of the heat-load problem.

References

Baron, A. Q. R. (1995). *Nucl. Instrum. Methods*, A**352**, 665–667.
Baron, A. Q. R., Kohmura, Y., Ohishi, Y. & Ishikawa, T. (1999). *Appl. Phys. Lett.* **74**, 1491–1494.
Berman, L. E. & Hart, M. (1991). *Nucl. Instrum. Methods*, A**300**, 415–421.
Bilderback, D. H. (1986). *Nucl. Instrum. Methods*, A**246** 434–436.
Bilderback, D. H., Freund, A. K., Knapp, G. S. & Mills, D. M. (2000). *J. Synchrotron Rad.* **7**, 53–60.
Carpentier, P., Rossat, M, Charrault, P., Joly, J., Pirrocchi, M., Ferrer, J.-L., Kaïkati, O. & Roth, M. (2001). *Nucl. Instrum. Methods*, A**456**, 163–176.
Chrzas, J., Khounsary, A. M., Mills, D. M. & Viccaro, P. J. (1990). *Nucl. Instrum. Methods*, A**291**, 300–304.
Chubar, O. & Elleaume, P. (1998). *Proceedings of the Sixth European Particle Accelerator Conference (EPAC98)*, pp. 1177–1179. Bristol: Institute of Physics.
Chumakov, A. I., Rüffer, R., Leupold, O., Barla, A., Thiess, H., Asthalter, T., Doyle, B. P., Snigirev, A. & Baron, A. Q. R. (2000). *Appl. Phys. Lett.* **77**, 31–33.
Ishikawa, T., Yamazaki, H., Tamasaku, K., Yabashi, M., Kuroda, M. & Goto, S. (1998). *Proc. SPIE*, **3448**, 2–10.
Khounsary, A., Yun, W., Trakhtenberg, E., Xu, S., Assoufid, L. & Lee, W. K. (1996). *Proc. SPIE*, **2855**, 266–275.
Lee, W. K., Fernandez, P. & Mills, D. M. (2000). *J. Synchrotron Rad.* **7**, 12–17.
Lee, W. K., Fezzaa, K., Fernandez, P., Tajiri, G. & Mills, D. M. (2001). *J. Synchrotron Rad.* **8**, 22–25.
Marot, G., Rossat, M., Freund, A., Joksch, S., Kawata, H., Zhang, L., Ziegler, E., Berman, L., Chapman, D., Hastings J. B. & Iarocci, M. (1992). *Rev. Sci. Instrum.* **63**, 477–480.
Mocella, V., Lee, W. K., Tajiri, G., Mills, D., Ferrero, C. & Epelboin, Y. (2003). *J. Appl. Cryst.* **36**, 129–136.
Oversluizen, T., Matsushita, M., Ishikawa T., Stefan, P. M., Sharma, S. & Mikuni, A. (1989). *Rev. Sci. Instrum.* **60**, 1493–1500.
Rüffer, R. & Chumakov, A. I. (1996). *Hyperfine Interact.* **97**/**98**, 589–604.
Snigirev, A., Kohn, V. K., Snigireva, I. & Lengeler, B. (1996). *Nature (London)*, **384**, 49–51.
Subbotin, V. I., Kolesov, V. S., Kuzmin, Yu. A. & Kharitonov, V. V. (1988). *Sov. Phys. Dokl.* **33**, 633–635.
Tajiri, G., Lee, W. K., Fernandez, P., Mills, D., Assoufid, L. & Amirouche, F. (2001). *J. Synchrotron Rad.* **8**, 1140–1148.
Tamasaku, K., Yabashi, M., Miwa, D., Mochizuki, T. & Ishikawa, T. (2002). *Proc. SPIE*, **4782**, 132–142.
Zhang, L., Hoszowska, J., Migliore, J.-S., Mocella, V., Ferrero, C. & Freund, A. K. (2001). *Nucl. Instrum. Methods*, A**467**/A**468**, 409–412.
Zhang, L., Lee, W.-K., Wulff, M. & Eybert, L. (2003). *J. Synchrotron Rad.* **10**, 313–319.

 Received 21 July 2003 • Accepted 24 November 2003